RPE | Radiation Physics & Engineering
A Peer-Reviewed Journal
Published by K.N. Toosi University of Technology
http://rpe.kntu.ac.ir
Research Article

Radiation Physics and Engineering 2026; ?(?):?–?

# Computational and experimental analysis of neutron radiography images for Aluminum- and Polyethylene-based samples

Zohreh Gholamzadeh*, Behrooz Rokrok, Reza Ebrahimzadeh, Hamid Saebi, Pooneh Tayyebi, Mohammad Hossein Mansoori, Mojtaba Afshani

*Nuclear Science and Technology Research Institute, Tehran, Iran*

## HIGHLIGHTS

- Neutron radiography is a useful tool to develop the industry and research needs.
- TRR radiography laboratory with neutron/gamma beam is used for image formation of different samples.
- Simulation methods well predict the sample image before practical tests.
- Both film-based and digital-based neutron radiography methods are used to obtain an image with the best quality.

## ABSTRACT

Neutron radiography is a powerful nondestructive imaging technique widely used at research reactors for industrial and scientific applications. In this study, image formation in neutron radiography was investigated using both computational and experimental approaches. The MCNPX Monte Carlo code was employed to simulate image formation in the film emulsion layer for polyethylene (PE) and aluminum (Al) samples irradiated by the neutron beam of the Tehran Research Reactor (TRR). The samples contained 1-mm-diameter holes filled with air, iron, copper, tin, and lead to evaluate image contrast and spatial resolution. The results show that the sample-converter-film configuration provides superior image quality for the investigated samples. Moreover, the spatial distribution of the $(n, \gamma)$ reaction rate in the gadolinium converter accurately predicts the radiographic image produced by transmitted neutrons before experimental irradiation. Experimental measurements indicate that the MX125 radiographic film provides higher image contrast and spatial resolution than the CCD-based digital imaging system, whereas the latter significantly reduces imaging time and enables digital image processing and three-dimensional reconstruction.

## KEYWORDS

Neutron radiography
Image formation
Monte Carlo simulation
Silver-based X-ray film
Digital CCD imaging

## HISTORY

Received:
Revised:
Accepted:
Published:

## 1 Introduction

Neutron radiography is a powerful non-destructive imaging technique used to examine the internal structure of a wide variety of objects. Unlike X-rays, whose attenuation generally increases with atomic number, the attenuation of thermal neutrons varies irregularly across the periodic table. Consequently, neighboring elements may exhibit significantly different neutron attenuation characteristics, making neutron radiography particularly effective for distinguishing materials that are difficult to differentiate using conventional X-ray imaging. In film-based neutron radiography, a gadolinium conversion screen is used to absorb incident neutrons. The subsequent emission of conversion electrons from the activated gadolinium screen exposes the adjacent radiographic film, thereby producing the latent image that is later developed chemically (Domanus, 1987).

It has been reported that approximately 95% of incident thermal neutrons are absorbed by a 25-$\mu$m-thick gadolinium converter. Following neutron capture, gadolinium emits conversion electrons with penetration ranges of approximately 50-100 $\mu$m. These ranges are well matched to the grain size of conventional radiographic films, allowing high spatial resolution to be achieved. In a typical film-based neutron radiography system, the sample, gadolinium converter, and conventional X-ray film are enclosed within an aluminum cassette and maintained in close contact throughout neutron irradiation to ensure optimum image quality (Pugliesi and Lehmann, 2005).

*Corresponding author: zgholamzadeh@aeoi.org.ir

https://doi.org/

Although digital neutron radiography (DNR), employing CCD cameras or flat-panel detectors, has largely replaced conventional film because of its rapid image acquisition and processing capabilities, film neutron radiography (FNR) continues to offer distinct advantages in applications requiring very high spatial resolution or large imaging areas. In particular, superior spatial resolution remains one of the principal advantages of film-based neutron radiography (Chankow et al., 2010; Alvarado et al., 2024).

Nuclear research reactors provide the most suitable neutron sources for radiographic imaging because they deliver sufficiently intense thermal neutron fluxes, enabling high-quality images to be acquired within relatively short exposure times.

Neutron radiography has found numerous industrial and scientific applications. For example, aluminum is relatively transparent to thermal neutrons, whereas corrosion products, particularly oxides, exhibit much higher neutron attenuation. Consequently, neutron radiography can reveal corrosion hidden beneath metallic surfaces. In this context, Zheng et al. (Zheng et al., 2017) investigated aluminum alloy hemmed joints using neutron radiography to visualize internal void formation.

Another important application is the non-destructive examination of archaeological artifacts. Neutron radiography enables visualization of internal organic components, such as wooden cores or paint layers, enclosed within metallic objects without damaging the artifact. For example, neutron and X-ray radiographs of a sixteenth-century wheel-lock pistol demonstrated complementary imaging capabilities. While the lead bullet inside the barrel was clearly visible in the X-ray radiograph, neutron radiography successfully revealed the surrounding gunpowder, corrosion products, and accumulated mud that were not distinguishable using X-rays alone (Rant et al., 2006).

The unique sensitivity of neutron radiography to hydrogen-rich materials also makes it particularly valuable for corrosion studies, nuclear fuel inspection, and moisture distribution analysis.

Wei et al. (Wei et al., 2015) compared conventional X-ray film with an X-ray imaging plate (IP) as neutron image detectors at the NEUTRA facility of the Paul Scherrer Institute. Their results demonstrated that both detection systems successfully identified intentionally introduced defects within a dummy nuclear fuel rod.

Chankow et al. (Chankow et al., 2010) compared neutron radiographs of a floppy disk acquired using a gadolinium/X-ray film system and a digital imaging system. Their results showed that the digital technique reduced imaging time by approximately a factor of forty while providing spatial resolution comparable to that of the film-based method.

More recently, Alvarado et al. (Alvarado et al., 2024) investigated pyrotechnic lines with diameters of approximately 640 $\mu$m containing microcracks using both silver-based radiographic films and digital imaging systems. Their results demonstrated that silver-based films remain highly competitive for obtaining high-spatial-resolution (approximately 50 $\mu$m) images over large inspection areas when only two-dimensional imaging is required. Although CCD-based systems equipped with thin scintillator screens can achieve comparable or even superior spatial resolution, this improvement is generally accompanied by reduced detection sensitivity and a considerably smaller field of view.

The objective of the present study is to perform both computational and experimental investigations of neutron radiographic imaging for aluminum- and polyethylene-based samples containing inserts made of different materials. The experimental measurements serve as the reference for validating the computational model. Comparison of the experimentally acquired radiographs with the simulated results enables assessment of the accuracy of the neutron cross-section data, radiation transport calculations, and geometric modeling implemented in the MCNPX code. Aluminum and polyethylene were deliberately selected because they exhibit substantially different neutron interaction characteristics. Polyethylene, owing to its high hydrogen content, strongly scatters and moderates thermal neutrons, whereas aluminum provides relatively low neutron attenuation and serves as a structural reference material. These contrasting properties provide an appropriate basis for evaluating the capabilities of both film-based and digital neutron radiography techniques.

## 2 Material and Methods

The Tehran Research Reactor (TRR) is equipped with a neutron radiography facility that supports both digital and film-based imaging techniques. In the present study, a computational model of the TRR radial neutron radiography beamline was developed using the MCNPX version 2.7.0 Monte Carlo code. The reactor core and the corresponding radial beam channel were modeled in detail. Neutron transport calculations were performed in KCODE mode to obtain the neutron and gamma-ray energy spectra at the exit of the neutron radiography beamline. MCNPX is a general-purpose Monte Carlo radiation transport code capable of simulating the transport of neutrons, photons, electrons, and other charged particles. Owing to its ability to accurately model particle interactions in complex geometries, it has been extensively applied in the design, optimization, and analysis of nuclear reactors, accelerator facilities, medical imaging systems, and neutron radiography installations (Pelowitz, 2008). The neutron and gamma-ray spectra were calculated at the tally position illustrated in Fig. 1. The F4 tally of MCNPX was employed to calculate the neutron and gamma-ray fluxes over the predefined energy groups. The resulting neutron and gamma-ray spectra were subsequently used as source definitions through the SDEF card in a second simulation stage, in which only the imaging geometry-including the sample, gadolinium converter, and radiographic film-was modeled and exposed separately to the neutron and gamma-ray sources (Fig. 2).

Uncorrected Proof

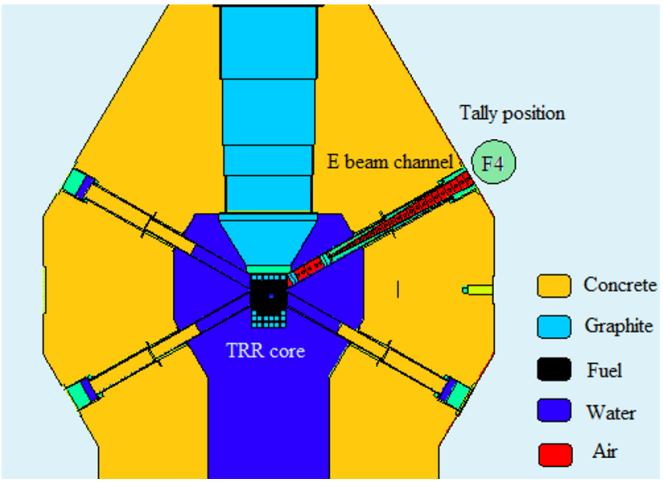


**Figure 1:** Schematic representation of the TRR neutron radiography beamline and the location used for neutron and gamma-ray spectrum calculations.

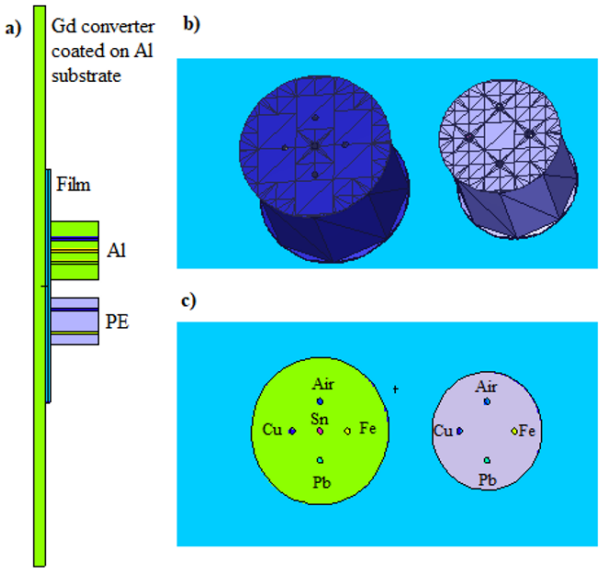


**Figure 2:** MCNPX model of the polyethylene- and aluminum-based samples: (a) axial view, (b) three-dimensional view showing the aluminum sample containing five 1-mm holes and the polyethylene sample containing four 1-mm holes, and (c) cross-sectional view of the modeled samples.

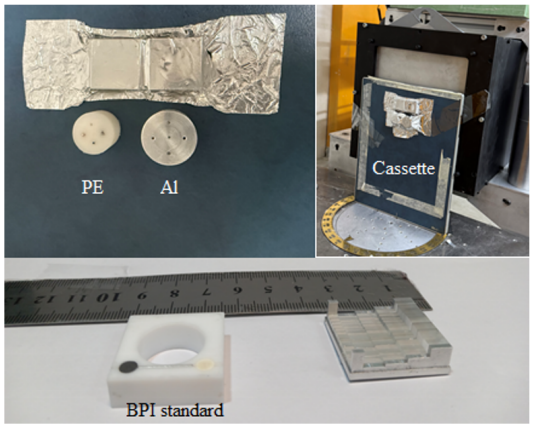


**Figure 3:** Experimental setup used for film-based and CCD-based neutron radiography.

The aluminum sample had a diameter of 2.5 cm and a height of 2 cm, and contained five 1-mm-diameter holes filled with lead, copper, iron, tin, and air. The polyethylene sample had a diameter of 2.0 cm and a height of 2 cm, and contained four 1-mm-diameter holes filled with lead, copper, iron, and air.

Materials possessing high neutron absorption cross sections (e.g., boron or cadmium) generally appear as dark regions because of their low neutron transmission. Materials with moderate neutron attenuation, such as lead or steel, exhibit intermediate contrast, whereas low-interaction materials, including air, appear nearly transparent relative to the surrounding matrix.

The mesh tally capability of MCNPX was used to calculate the $(n, \gamma)$ reaction rate within the gadolinium converter. This reaction-rate distribution represents the neutron transmission map of the sample and corresponds to the image that is ultimately transferred to the emulsion layer of the radiographic film.

The radiographic film emulsion consists of silver halide crystals (primarily AgBr and AgCl) dispersed within a gelatin matrix. During neutron irradiation, the Gd-158 isotope captures thermal neutrons and is converted to excited Gd-159, which subsequently emits internal conversion electrons. These electrons expose the silver halide crystals in a manner analogous to X-ray exposure, thereby producing the latent image that becomes visible after chemical development.

The silver-based radiographic film was modeled with the following layer structure (Blanton, 2003):

Cardboard backing: 1.0 mm
Lead coating: 27.5 $\mu$m
Film base: 175 $\mu$m
Emulsion layer: 12.5 $\mu$m
Gelatin protective layer: 1.5 $\mu$m

For gamma-ray simulations, the deposited energy within the emulsion layer was calculated using the mesh tally together with the PEDEP option of MCNPX. This tally represents the energy deposited by photons and their secondary charged particles inside the sensitive emulsion volume. Energy deposition by both primary gamma rays and secondary electrons generated during gamma interactions was included in the calculations.

For the primary radiation sources defined through the SDEF card, the neutron and gamma-ray beams were assumed to be nearly parallel with a divergence angle of approximately 2°, consistent with the characteristics of the TRR neutron radiography beamline. The angular distribution of the incident particles was specified using the DIR parameter of the SDEF card. In contrast, all secondary particles generated during neutron and gamma interactions were automatically produced and transported by MCNPX according to the underlying nuclear interaction physics.

To evaluate the contribution of different particles to image formation, separate calculations were performed for neutron energy deposition, neutron-induced secondary photons, neutron-induced electrons, when the radiation source is neutron.

Because the TRR E-beam channel has a direct line of

Under review Proof

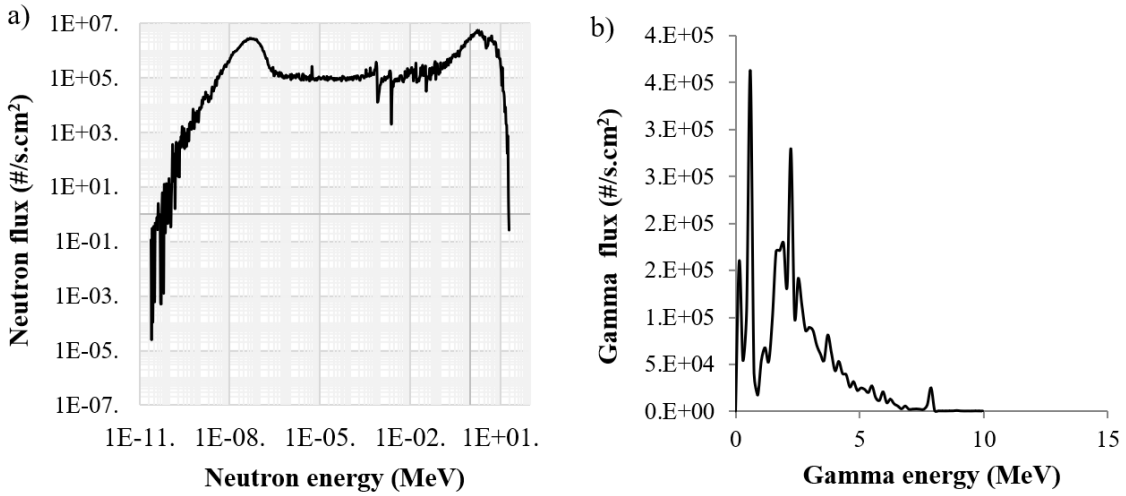


**Figure 4:** Calculated neutron and gamma-ray spectra at the exit of the TRR E-beam channel: (a) neutron spectrum and (b) gamma-ray spectrum.

sight to the reactor core, a relatively intense gamma-ray component reaches the imaging position. Consequently, the deposited energies resulting from reactor-core gamma rays and gamma-induced secondary electrons were explicitly calculated within the film emulsion when the radiation source is gamma.

Following neutron transmission through the sample, the neutron intensity distribution activates the gadolinium converter, producing a spatial distribution of Gd-159 nuclei. The conversion electrons emitted from these activated nuclei constitute the dominant mechanism responsible for image formation in film-based neutron radiography. Accordingly, the spatial distribution and energy spectrum of these electrons were employed as source terms in the MCNPX simulations to calculate the deposited energies associated with primary conversion electrons and the secondary photons generated by electron transport.

All deposited-energy calculations were performed using the F6 tally. For each sample, only the corresponding contact area between the sample and the radiographic film was modeled to eliminate contributions from regions of the film that were not directly involved in image formation.

Experimental neutron radiography was carried out at a reactor power of 4.5 MW. Exposure times of 16 min for film-based imaging and 10 min for CCD-based imaging were selected according to the experimental arrangement shown in Fig. 3. Both digital and film-based neutron radiographs were acquired for comparison with the computational predictions.

## 3 Result and Discussion

The neutron and gamma-ray spectra at the exit of the TRR neutron radiography beamline were calculated using the F4 tally of the MCNPX code. The calculated spectra are presented in Fig. 4. The relative statistical uncertainties of the Monte Carlo calculations at the tally position were below 10%, at the tally position or the beam line exit of the TRR reactor indicating acceptable statistical convergence for the subsequent image simulations.

In film-based neutron radiography, image formation results from the combined contributions of several radiation components, including transmitted neutrons, neutron-induced secondary gamma rays, neutron-induced electrons, reactor-core gamma rays, gamma-induced electrons, and conversion electrons emitted from activated gadolinium.

The deposited energy associated with each particle type was calculated using the F6 tally and is summarized in Tables 1 and 2 for aluminum and polyethylene samples, respectively. These values represent the energy deposited within the sensitive emulsion layer of the radiographic film and therefore provide a quantitative measure of the contribution of each particle to image formation.

As the neutron beam passes through the sample, it carries the attenuation pattern of the sample toward the gadolinium converter. Although a small fraction of the neutron energy is deposited directly within the emulsion layer, additional contributions originate from neutron-induced secondary particles and reactor-core gamma radiation. These secondary particles introduce image blurring and therefore influence the final image quality.

For the aluminum sample, the calculations indicate that the Gd-159 beta particle dominate the image formation process, accounting for more than 95% of the total deposited energy within the emulsion layer (Table 1). The contributions of neutrons, secondary photons, and secondary electrons are comparatively small and therefore have only a limited influence on the final radiographic image.

For the polyethylene sample, the conversion electrons emitted by Gd-159 remain the dominant contributors to image formation, accounting for approximately 71% of the total deposited energy. However, unlike the aluminum sample, neutron-induced secondary gamma rays contribute approximately 12%, indicating that secondary radiation plays a more significant role because of the stronger neutron scattering characteristics of polyethylene (Table 2).

Uncorrected Proof

**Table 1:** Deposited energy and relative contribution of different particles to image formation in the radiographic film emulsion for the aluminum sample.

| Primary source: neutron beam | | |
|---|---|---|
| Particle | Deposited energy ($MeV.s^{-1}$) | Weight on image formation (%) |
| n | 30.83E05 | 0.781 |
| p | 50.89E05 | 1.290 |
| e | 26.63E05 | 0.675 |
| Primary source: emerged-core gamma beam | | |
| p | 8.742E05 | 0.222 |
| e | 11.64E05 | 0.295 |
| Primary source: electron particles of Gd-159 beta emitter | | |
| p | 55.26E05 | 1.400 |
| e | 3761.52E05 | 95.30 |

**Table 2:** Deposited energy and relative contribution of different particles to image formation in the radiographic film emulsion for the polyethylene sample.

| Primary source: neutron beam | | |
|---|---|---|
| Particle | Deposited energy ($MeV.s^{-1}$) | Weight on image formation (%) |
| n | 3.569E05 | 2.110 |
| p | 19.72E05 | 11.60 |
| e | 10.01E05 | 5.910 |
| Primary source: emerged-core gamma beam | | |
| p | 8.160E05 | 4.820 |
| e | 6.272E05 | 3.700 |
| Primary source: electron particles of Gd-159 beta emitter | | |
| p | 1.625E05 | 0.957 |
| e | 120.0E05 | 70.90 |

When any particle interacts within the emulsion layer, it deposits energy, creating a "footprint" by altering the silver halide crystals. The code calculates the energy deposition of all particles -both primary and secondary- individually. These individual depositions are then summed to determine the total energy deposited within the emulsion layer. The contribution of each particle to image formation is then determined by dividing its individual energy deposition by this total value, as outlined in Tables 1-2. Standard 2D imaging using mesh tallies, however, does not inherently incorporate these particle weights. Consequently, the summation of images from all particle types is not performed. Based on Tables 1-2, it is evident that primary particles (neutrons and gamma rays originating from the reactor core) contribute most significantly to image formation.

It is well established that the $(n, \gamma)$ reaction rate within the gadolinium converter determines the radiographic representation of the sample when the neutron beam passes through the specimen and reaches the X-ray film positioned between the sample and the converter. The mesh tally results of the reaction rate in the 25 $\mu$m-thick gadolinium converter are presented in Fig. 5. Although the final radiographic image obtained after film development differs slightly from the calculated reaction-rate distribution, the latter provides the closest representation of the image formation process because the emitted beta particles originate directly from this spatial distribution.

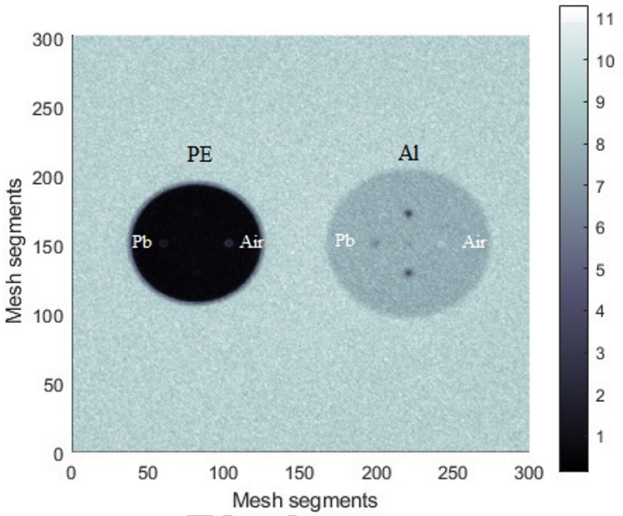


**Figure 5:** Radiographic image formed by the $(n, \gamma)$ reaction in the gadolinium converter during exposure to neutrons emerging from the TRR core.

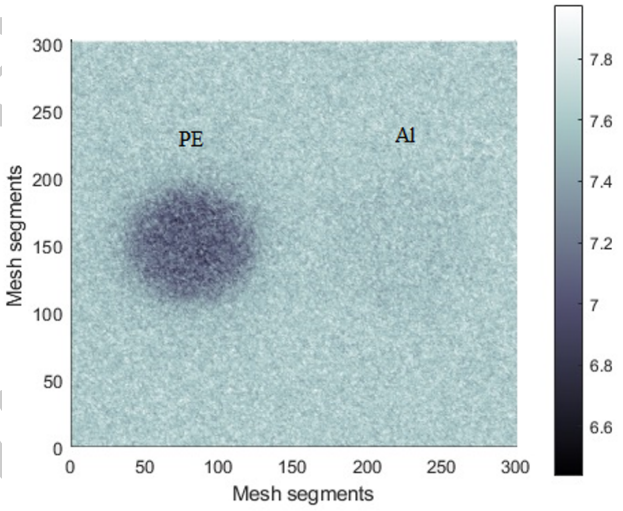


**Figure 6:** Spatial distribution of the image formed by secondary gamma rays in the emulsion layer during exposure to the neutron beam emerging from the TRR core.

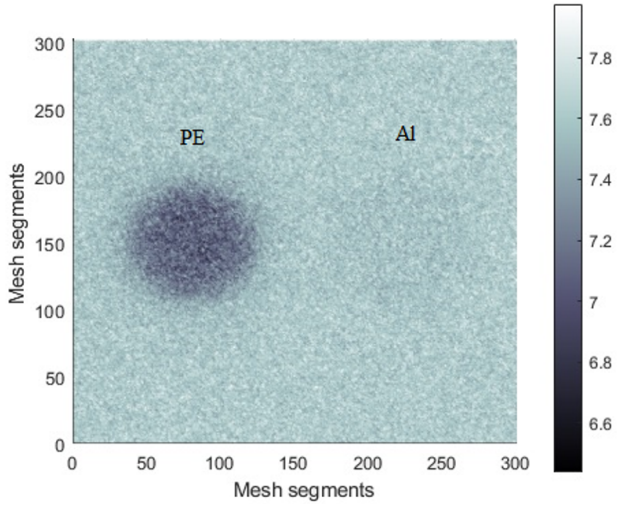


**Figure 7:** Spatial distribution of the image formed by gamma rays emerging from the TRR core in the emulsion layer.

Uncorrected Proof

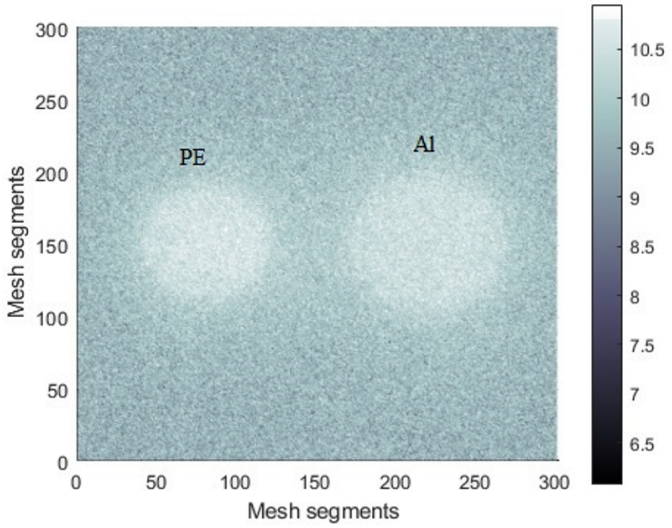


**Figure 8:** Radiographic image formed by gamma-induced secondary electrons in the emulsion layer during irradiation with gamma rays emerging from the TRR core.

The energy deposited in the emulsion layer by secondary gamma rays generated during neutron irradiation is presented in Fig. 6. In addition, gamma rays emerging directly from the Tehran Research Reactor (TRR) core also contribute to image formation, as illustrated in Fig. 7, which shows the corresponding energy deposition in the emulsion layer. The image produced by gamma-induced secondary electrons in the emulsion is shown in Fig. 8. Although these secondary electrons introduce a background component that may degrade image quality, their contribution to the overall image formation is considerably smaller than that of the beta particles emitted following neutron capture in 159Gd and the direct gamma radiation originating from the reactor core.

It should be noted that, for beta particles generated following neutron- or gamma-induced interactions, the Monte Carlo code automatically simulates their production, transport, and possible absorption. Consequently, the particles contributing to image formation are specified only through the MODE card. The user is therefore not required to define an explicit beta-particle energy spectrum. Instead, the primary neutron or gamma source is defined using the SDEF card, while all secondary particles produced through neutron or gamma interactions are generated and transported automatically according to the underlying physical interaction models implemented in the code.

Figure 9 presents the one-dimensional (1D) profile of the $(n,\gamma)$ reaction rate within the 25 $\mu$m-thick gadolinium converter. The profiles along the Y and Z directions, corresponding to the positions of the holes in the samples, clearly indicate that the polyethylene (PE) sample provides higher edge contrast than the aluminum (Al) sample, as aluminum is nearly transparent to thermal neutrons. In contrast, the image contrast of the Cu, Sn, and Pb inserts is higher in the aluminum sample than in the PE sample. This behavior can be attributed to the relatively large neutron scattering cross section of polyethylene, which degrades the contrast of these high-attenuation inserts.

Figure 10 shows the one-dimensional (1D) profiles of the gamma-ray energy deposited in the film emulsion layer. The profiles along the Y and Z directions, corresponding to the positions of the holes in the samples, indicate that the aluminum (Al) sample is expected to exhibit better edge contrast than the polyethylene (PE) sample because of its higher atomic number. In contrast, the contrast of all Cu, Sn, and Pb inserts is higher in the PE sample than in the Al sample due to the larger difference in atomic number between polyethylene and the insert materials.

It should be noted that image quality is not directly determined by the reactor power but rather by the neutron fluence delivered to the sample. Operating the reactor at a lower power level simply increases the irradiation time required to achieve the desired neutron fluence. In the experimental imaging performed in this study, the Tehran Research Reactor (TRR) was operated at a power of 4.5 MW. Under these conditions, the optimum image quality for the digital imaging system was obtained with a 10 min exposure using the CCD camera, whereas an exposure time of 16 min was required for the film-based radiography system. It should also be noted that the optimum exposure time depends strongly on the sample thickness and the characteristics of the radiographic film.

In the Monte Carlo simulations, however, reactor power is not a governing parameter for image formation. The simulation code tracks the transport and interactions of individual particles and reports the results on a per-source-particle basis. Consequently, each particle is assigned an independent statistical weight, and the predicted reaction rates and energy deposition distributions are normalized per source particle. Reactor power, which only determines the number of particles emitted per unit time, therefore acts solely as a scaling factor and does not influence the predicted image quality.

Table 3 and 4 shows point spread function (PSF-FWHM) of any hole in the core-emerged gamma and $(n,\gamma)$ formed images as the most powerful sources of image formation according to the previous discussions.

**Table 3:** $\mathrm{PSF_{FWHM}}$ of the holes inserted in polyethylene and aluminum samples calculated for $(n,\gamma)$ formed image.

| Hole | Polyethylene | Aluminum |
|---|---|---|
| Pb | 0.4651 | 0.1588 |
| Air | 0.5293 | 0.2890 |
| Fe | 0.7970 | 0.1411 |
| Cu | 0.6373 | 0.1173 |
| Sn | - | 0.4311 |

**Table 4:** $\mathrm{PSF_{FWHM}}$ of the holes inserted in polyethylene and aluminum samples calculated for core-emerged gamma formed image.

| Hole | Polyethylene | Aluminum |
|---|---|---|
| Pb | 0.1053 | 0.1075 |
| Air | 0.1144 | 0.1183 |
| Fe | 0.1033 | 0.1029 |
| Cu | 0.1041 | 0.1001 |
| Sn | - | 0.1024 |

Uncorrected Proof

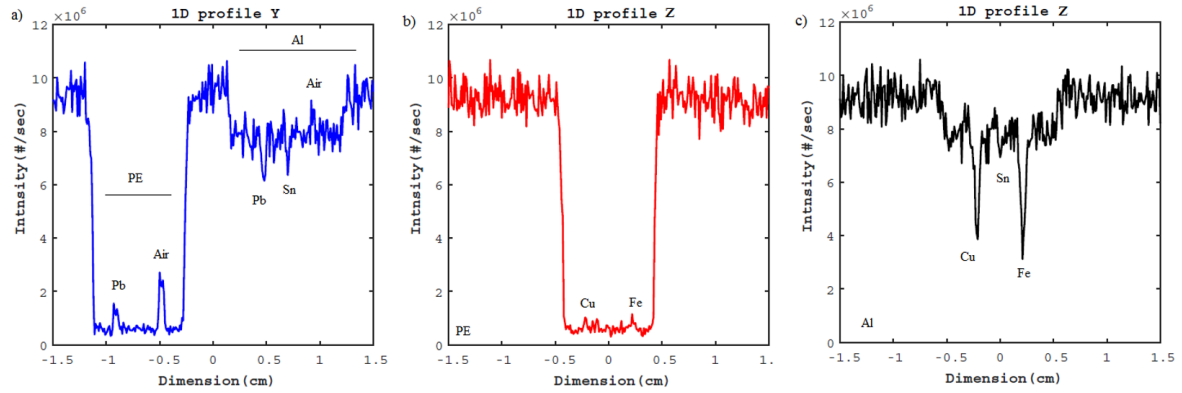


**Figure 9:** One-dimensional (1D) profiles of the $(n, \gamma)$ reaction rate in the gadolinium converter during irradiation with neutrons emerging from the TRR core: (a) Y-axis profiles for the aluminum and polyethylene samples, (b) Z-axis profile for the polyethylene sample, and (c) Z-axis profile for the aluminum sample.

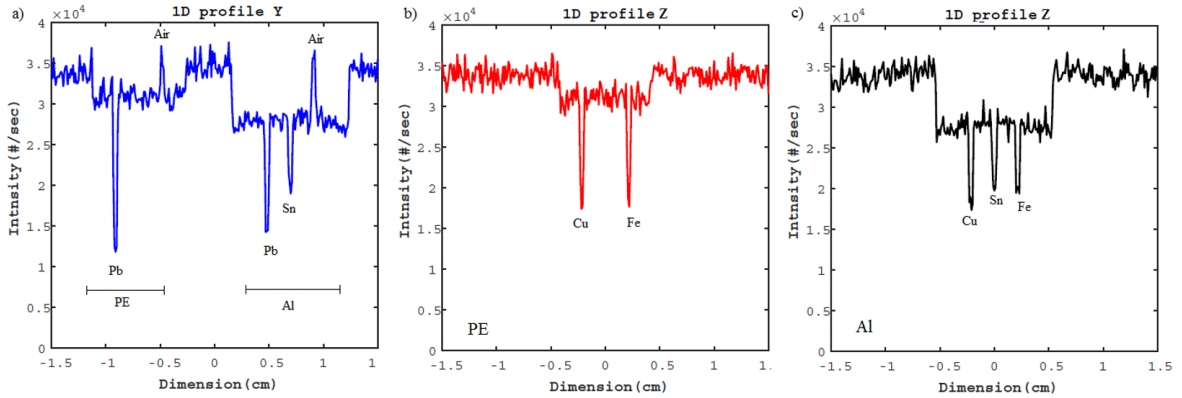


**Figure 10:** One-dimensional (1D) profiles of the gamma-ray energy deposited in the film emulsion layer during irradiation with gamma rays emerging from the TRR core: (a) Y-axis profiles for the aluminum and polyethylene samples, (b) Z-axis profile for the polyethylene sample, and (c) Z-axis profile for the aluminum sample.

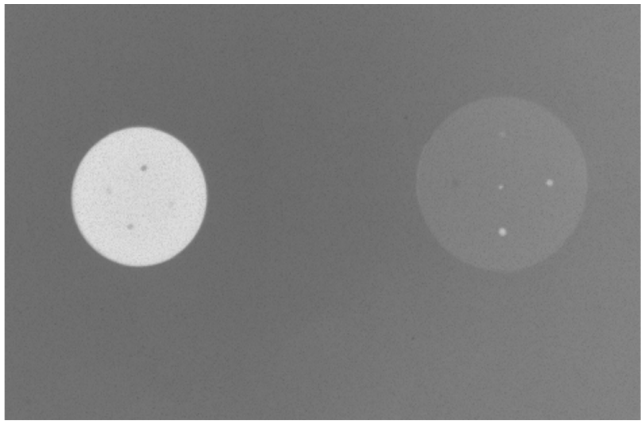

**Figure 11:** Digital neutron radiographic image of the samples acquired using a CCD camera during irradiation with the neutron/gamma beam emerging from the TRR core (10 min exposure time).

The calculated PSFFWHM of the holes in the formed images shows due to high neutron scattering of the polyethylene sample, neutron radiography of an aluminum sample would consequence in better images with sharper contrast and resolution. Also for both the investigated samples, the calculated PSFFWHM of the holes are noticeably improved in the gamma-induced images than the neutron-induced images; especially in the case of polyethylene sample.

Figure 11 shows the digital neutron radiographic image of the samples acquired using the CCD camera with an exposure time of 10 min.

Figure 12 shows the neutron radiographic image of the samples obtained using the film-based imaging technique with an exposure time of 16 min. In this arrangement, the MX125 radiographic film was positioned between the sample and the gadolinium converter, corresponding to the back configuration.

Neutron radiography is inherently time-consuming and costly because experimental imaging requires the operation of a nuclear research reactor. Consequently, computational simulation provides an efficient approach for predicting image quality prior to performing expensive irradiation experiments. To the best of our knowledge, the individual contributions of the various particles involved in image formation within radiographic films have not previously been investigated in a systematic manner. In the present study, image formation is analyzed without relying on the radiography tally implemented in the MCNPX code, as this tally does not explicitly account for the in-

fluence of the film-converter assembly on the image formation process. Instead, the proposed methodology enables a detailed evaluation of the contributions of neutrons, capture-generated beta particles, gamma rays, and secondary electrons to the final radiographic image.

The results provide practical guidance for researchers in selecting appropriate simulation methodologies and optimizing imaging system configurations prior to experimental implementation. Furthermore, CCD-based neutron imaging systems offer the additional capability of three-dimensional (3D) image reconstruction through digital image processing and tomographic reconstruction techniques, which cannot be achieved using conventional film-based radiography. It should also be emphasized that film-based imaging does not necessarily provide superior image quality. The optimum imaging technique depends strongly on the material composition and thickness of the inspected sample. Consequently, under certain conditions, CCD-based imaging systems can outperform conventional film-based methods while simultaneously providing the significant advantage of three-dimensional imaging capability.

## 4 Conclusions

Neutron radiography is a valuable nondestructive testing technique with broad applications in industry, research, and scientific development. In the present study, both computational and experimental approaches were employed to investigate the neutron radiographic imaging of aluminum and polyethylene samples irradiated by the neutron/gamma beam of the Tehran Research Reactor (TRR) radiography facility.

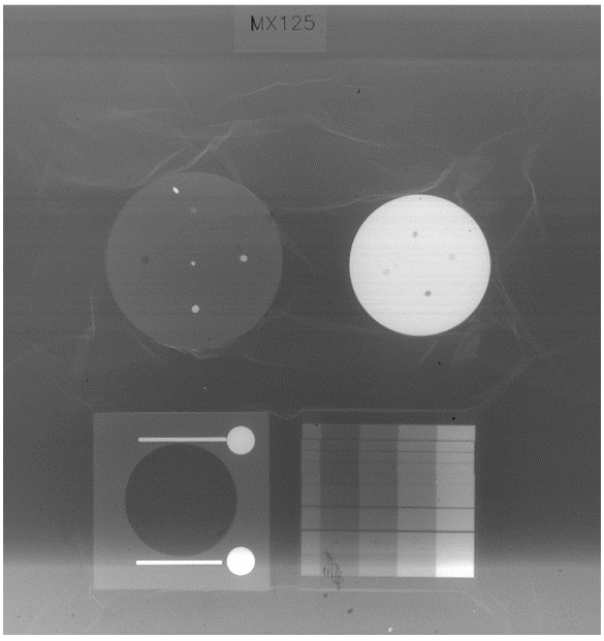


**Figure 12:** Film-based neutron radiographic image of the samples acquired with the MX125 radiographic film in the back configuration during irradiation with the neutron/gamma beam emerging from the TRR core (16 min exposure time).

The simulation results demonstrated that the radiographic image can be reliably predicted prior to experimental measurements, thereby reducing the time and cost associated with reactor-based imaging. The calculations further showed that the spatial distribution of the $(n, \gamma)$ reaction rate within the gadolinium converter and the energy deposited by gamma rays emerging from the TRR core in the film emulsion layer are the dominant contributors to image formation. The contributions of other secondary particles were found to be comparatively small and, in most cases, negligible.

The results also indicate that the selection of the film-converter configuration should be based on the material properties of the inspected sample. In the conventional sample-converter-film configuration, image formation is dominated by beta particles generated through neutron capture in the gadolinium converter. In contrast, in the sample-film-converter (back-configuration) arrangement, the contribution of gamma rays emerging from the reactor core becomes more significant than the contribution of the $(n, \gamma)$ reaction products.

Experimental results showed that, under the investigated conditions, the film-based imaging system produced higher image quality than the CCD-based system. However, the CCD-based technique substantially reduced the required imaging time and additionally provides the capability for three-dimensional (3D) image reconstruction, making it an attractive alternative for many practical applications.

It should be emphasized that, in routine radiographic inspections, the objective is generally to identify defects such as cracks, voids, or inclusions exceeding specified acceptance criteria. Therefore, image evaluation is primarily based on qualitative visual inspection rather than quantitative image analysis. In the present work, image quality was assessed by comparing the visibility of the holes in both the simulated and experimental radiographs. The excellent agreement between the computational predictions and the experimental results confirms the validity of the proposed simulation methodology. Consequently, the developed computational approach can serve as an effective tool for selecting the most appropriate imaging configuration, whether film-based or CCD-based, while minimizing experimental time, reactor utilization, and associated costs.

## Conflict of Interest

The authors declare no potential conflict of interest regarding the publication of this work.

## Funding

The authors declare that no funds, grants, or other financial support were received during the preparation of this manuscript.

Uncorrected Proof

## References


Alvarado, K., Drouart, A., and Ott, F. (2024). Comparison of resolution and contrast performances of silver film, imaging plate and scintillator images in neutron radiography. In *EPJ Web of Conferences*, volume 298, page 02002. EDP Sciences.

Blanton, T. (2003). X-ray film as a two-dimensional detector for X-ray diffraction analysis. *Powder Diffraction*, 18(2):91–98.

Chankow, N., Punnachaiya, S., and Wonglee, S. (2010). Neutron radiography using neutron imaging plate. *Applied Radiation and Isotopes*, 68(4-5):662–664.

Domanus, J. (1987). *Recording Radiographic Images on Nitrocellulose Film in Neutron Radiography of Nuclear Reactor Fuel*. Risø National Laboratory.

Pelowitz, D. (2008). MCNPX user's manual, version 2.6. 0, LA-CP-07-1473. *Los Alamos Natl Lab Los Alamos*.

Pugliesi, R. and Lehmann, E. (2005). Neutron-induced electron radiography using an imaging plate. *Applied Radiation and Isotopes*, 62(3):457–460.

Rant, J., Milič, Z., Istenič, J., et al. (2006). Neutron radiography examination of objects belonging to the cultural heritage. *Applied Radiation and Isotopes*, 64(1):7–12.

Wei, G., Han, S., Wang, H., et al. (2015). Experience of the indirect neutron radiography method based on the x-ray imaging plate at CARR. *Physics Procedia*, 69:258–264.

Zheng, S., Vanderstelt, J., McDermid, J., et al. (2017). Non-destructive investigation of aluminum alloy hemmed joints using neutron radiography and X-ray computed tomography. *NDT & E International*, 91:32–35.



©2026 by the journal.

RPE is licensed under a Creative Commons Attribution-NonCommercial 4.0 International License (CC BY-NC 4.0).



**To cite this article:**

Z. Gholamzadeh, B. Rokrok, R. Ebrahimzadeh, H. Saebi, P. Tayyebi, M. H. Mansoori, M. Afshani. Computational and experimental analysis of neutron radiography images for Aluminum- and Polyethylene-based samples. *Radiation Physics and Engineering*, In Press.

DOI:

To link to this article:


Unedited Proof